

## Vertical Structure of Convective Systems during NAME 2004

DAVID G. LERACH, STEVEN A. RUTLEDGE, CHRISTOPHER R. WILLIAMS,\* AND ROBERT CIFELLI<sup>†</sup>

*Department of Atmospheric Science, Colorado State University, Fort Collins, Colorado*

(Manuscript received 12 May 2009, in final form 9 November 2009)

### ABSTRACT

This study describes the vertical structure of mesoscale convective systems (MCSs) that characterized the 2004 North American monsoon utilizing observations from a 2875-MHz (S band) profiler and a dual-polarimetric scanning Doppler radar. Both instrument platforms operated nearly continuously during the North American Monsoon Experiment (NAME). A technique was developed to identify dominant hydrometeor type using S-band (profiler) reflectivity along with temperature. The simplified hydrometeor identification (HID) algorithm matched polarimetric scanning radar fuzzy logic-based HID results quite well. However, the simplified algorithm lacked the ability to identify ice hydrometeors below the melting layer and on occasion, underestimated the vertical extent of graupel because of a profiler reflectivity bias.

Three of the strongest NAME convective rainfall events recorded by the profiler are assessed in this study. Stratiform rain exhibited a reflectivity bright band and strong Doppler velocity gradient within the melting layer. Convective rainfall exhibited high reflectivity and Doppler velocities exceeding 3 ( $-10$ )  $\text{m s}^{-1}$  in updrafts (downdrafts). Low-density graupel persisted above the melting layer, often extending to 10 km, with high-density graupel observed near  $0^{\circ}\text{C}$ . Doppler velocity signatures suggested that updrafts and downdrafts were often tilted, though estimating the degree of tilt would have required a more three-dimensional view of the passing storms. Cumulative frequency distributions (CFDs) of reflectivity were created for stratiform and convective rainfall and were found to be similar to results from other tropical locations.

### 1. Introduction

The North American Monsoon Experiment (NAME) field campaign was held from June through September of 2004 and aimed to improve the predictability of warm-season precipitation over North America. The efforts sought an increased understanding of the physical processes that control the regional climate and its associated modes of variability, both seasonal and interannual (Higgins et al. 2006).

The NAME tier-I region (Higgins et al. 2006) consisted primarily of the Baja California Peninsula, the Gulf of California, southwestern United States, and western

Mexico, including the western flanks of the Sierra Madre Occidental (SMO) mountain range (Fig. 1). During the NAME enhanced observation period (EOP) in July and August of 2004, observations were made from a multi-radar network within the tier-I region (Lang et al. 2007). The primary radar, the National Center for Atmospheric Research (NCAR) S-Pol dual-polarimetric scanning Doppler radar, was situated roughly 100 km north of Mazatlán, Mexico, on the Gulf of California coast ( $23.93^{\circ}\text{N}$ ,  $106.95^{\circ}\text{W}$ ). The National Oceanic and Atmospheric Administration (NOAA) Aeronomy Laboratory (AL) and NOAA Environmental Technology Laboratory (ETL)<sup>1</sup> operated a field site containing wind-profiling radars, precipitation-profiling radars, surface upward-downward radiation instruments, a tipping-bucket rain gauge, and other surface instruments (Williams et al. 2007). The site ( $24.28^{\circ}\text{N}$ ,  $107.16^{\circ}\text{W}$ ) was situated approximately 45 km northwest of the S-Pol radar, allowing for coordinated profiler/S-Pol radar observations. The

\* Additional affiliation: Cooperative Institute for Research in Environmental Sciences, University of Colorado, Boulder, Colorado.

<sup>†</sup> Current affiliation: Cooperative Institute for Research in the Atmosphere, NOAA/Earth System Research Laboratory, Boulder, Colorado.

*Corresponding author address:* David G. Lerach, Department of Atmospheric Science, Colorado State University, Fort Collins, CO 80523.

E-mail: dlerach@atmos.colostate.edu

<sup>1</sup> Since October 2005, NOAA AL and NOAA ETL were merged into the NOAA Earth System Research Laboratory (ESRL) and personnel who participated in the NAME 2004 field campaign are now members of the Physical Sciences Division.

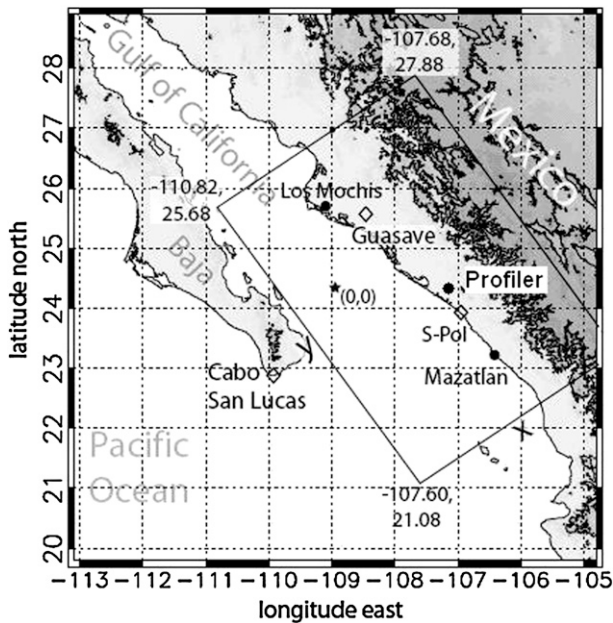


FIG. 1. Map of the instrument platforms within the NAME tier-I region. The S-Pol radar was located just west of La Cruz, Mexico, while the NOAA profiler site was placed roughly 45 km to the northwest in Sinaloa. Two SMN radars are also marked with diamonds (adapted from Lang et al. 2007). The inscribed subdomain was used for reduced-dimension analyses in Lang et al. (2007).

locations of both the S-Pol radar and NOAA field site are shown in Fig. 1. Since both instrument sites were situated on the coastal plain, unobstructed views over the profiler by the S-Pol radar could be obtained.

One particular focus of NAME was documenting the detailed physical structure and kinematics of mesoscale convective systems (MCSs; Higgins et al. 2006). Lang et al. (2007), in performing a reduced dimension analysis within the subdomain of the tier-I region (Fig. 1), confirmed that MCSs were the dominant mode of convective rainfall within the core domain of the North American monsoon. However, that study focused primarily on the statistical properties of MCSs observed during NAME with the scanning radar network as opposed to details of precipitation and echo structure within subregions of MCSs. The NOAA 2875-MHz (S-band) vertically pointing profiler radar situated at the NOAA field site possessed significantly greater vertical and temporal resolution than that of the Mexican Servicio Meteorológico Nacional (SMN) radars. The primary goals of this study were to assess the detailed vertical structure of MCSs observed during NAME as observed by the NOAA S-band profiler radar and to place these analyses in context with larger-scale measurements made by the S-Pol radar. Emphasis was placed on identifying kinematic structure and microphysical processes. To accomplish this

goal, it was necessary to develop a nonpolarimetric hydrometeor identification (HID) algorithm that could be applied directly to the profiler data. Past studies have utilized reflectivity and radial velocity data from 915-MHz and 3-GHz profiler radars to examine the vertical structure of precipitating cloud systems (e.g., Williams et al. 1995; Ecklund et al. 1999; Gage et al. 1994, 1999, 2000; Atlas and Williams 2003; May and Keenan 2005; Williams et al. 2007). This study goes one step further and makes use of how reflectivity can play a significant role in identifying dominant hydrometeor species in tropical rainfall. The HID procedure is described in the next section.

## 2. Data and methodology

### a. S-Pol radar

The NCAR S-Pol radar operates at S-band ( $\sim 3$  GHz or 10 cm) and provided both kinematic and microphysical information within precipitation systems that moved over the NAME tier-I domain from 5 July through 21 August. As described in Lang et al. (2007), the S-Pol operation utilized a variety of sampling strategies throughout NAME: both plan position indicator (PPI) and range height indicator (RHI) data were collected to provide information on the horizontal extent and the detailed vertical structure of precipitation. The scanning radar measured equivalent reflectivity, radial velocity, and spectral width, as well as the following polarimetric variables: differential reflectivity  $Z_{dr}$ , linear depolarization ratio (LDR), correlation coefficient at zero lag time  $\rho_{hv}$ , and differential phase  $\Phi_{dp}$ . The range-filtered specific differential phase  $K_{dp}$  was derived from  $\Phi_{dp}$ . When combined with reflectivity and temperature profiles (obtained from sounding data), the polarimetric variables were used to estimate bulk hydrometeor types using a fuzzy logic approach (Liu and Chandrasekar 2000). This study makes use of both the S-Pol surveillance scans as well as high-resolution RHI scans made over the profiler site. See Doviak and Zrnić (1993) and Bringi and Chandrasekar (2001) for a more complete discussion of the various radar polarimetric variables.

### b. NOAA 2875-MHz profiler

The NOAA 2875-MHz profiling radar operated nearly continuously from 30 July to 18 September during NAME. It measured equivalent reflectivity, Doppler velocity, and spectral width. The profiler operated in three modes: high-resolution (precipitation) mode, attenuated mode, and cloud mode. Each mode was characterized by changes in transmit pulse length and sensitivity settings (Williams et al. 2007). The profiler scans provided 45-s temporal resolution (15 s per mode).

This study used the dataset collected in the precipitation mode, which was characterized by a pulse length of  $0.4 \mu\text{s}$  and a gate spacing of 60 m. This provided for more detailed profiles of the vertical structure of precipitation overhead. The S-band profiler observed 8727 profiles from 23 rain events during NAME. For quality control methods and a more complete description of the NOAA S-band profiler radar see Williams et al. (2007). It should be noted that for this study, the S-band profiler dataset was further quality controlled with the application of a two-gate despeckling (Lang et al. 2005) algorithm. Spectral width was not analyzed in any detail in this study. However, spectral width was used in our precipitation-type classification algorithm.

### c. Methodology

This study included a new method of assessing the vertical structure of dominant hydrometeor species from the profiler data itself, without the need for polarimetric scanning radar data, which were not always available. Previous profiler-based studies have included HID analyses by interpolating S-band three-dimensional scanning radar-based diagnosed HID over the profiler location (e.g., May and Keenan 2005). While useful, S-band scanning radars generally have reduced vertical and temporal resolution over a specific location as compared to profilers. In the case of NAME, the S-band profiler scanned in precipitation mode every 45 s with 60-m vertical resolution while S-Pol completed single volume scans in its surveillance mode (Lang et al. 2005) approximately once every 10 min with relatively poor vertical resolution ( $>1\text{-km}$  resolution above 7 km typically). S-Pol RHI scans provided higher spatial and temporal resolution over the profiler than the surveillance scans. However, RHI scans were rarely made directly over the profiler. Additionally, S-Pol pulse volumes over the profiler site were more than 3 times larger than those of the S-band profiler (Fig. 2). Therefore, HID fields derived from S-Pol were at considerably lower spatial resolution compared to the native profiler data. Rather than solely relying on an S-Pol-based fuzzy logic-based approach (Liu and Chandrasekar 2000) to estimate hydrometeor types over the profiler, a new approach was taken, developing an HID algorithm that required only S-band profiler reflectivity data and temperature. The method was tuned, based on the polarimetric HID provided by S-Pol. The new method provided HID estimates over the profiler site with the same vertical and time resolution as the native profiler measurements. This HID methodology originally produced spurious results, which occurred most often in high reflectivity within stratiform brightband regions, where the HID would identify incorrect hydrometeor types such as graupel or hail. As

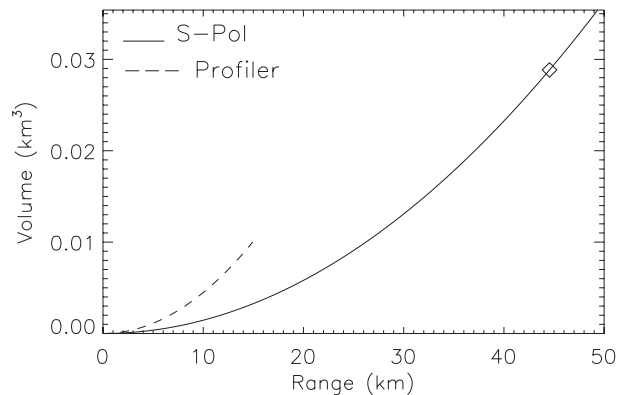


FIG. 2. Variation of pulse volume with range for the S-Pol radar (solid) and S-band profiler (dashed). The diamond plotted on the S-Pol curve depicts the approximate pulse volume of S-Pol measurements made over the profiler.

described below, solving this problem required reducing high reflectivity bias within stratiform brightband regions. This in turn, required the classification of each individual profile with a specific precipitation type.

The first step in analyzing the profiler data was to separate the individual profiles by precipitation type using a classification algorithm adapted from Williams et al. (1995). The algorithm separated the profiler dataset into four classifications: 1) stratiform, 2) convective, 3) mixed stratiform–convective, and 4) upper-level anvil clouds (cirrus). Of the 8727 profiles recorded from the profiler, 3671 were classified as stratiform, 749 as convective, 1588 as mixed stratiform/convective, and 2719 as cirrus. A full description of the classification algorithm is given in the appendix. Once each profile was assigned a precipitation type, the brightband reflectivity was filtered out of all stratiform profiles by linearly interpolating reflectivity within the layer from the actual reflectivity measurements at gates immediately above and below the bright band. An example of this process is shown in Fig. 3. Note that this brightband reflectivity filtering was only carried out when running the precipitation type algorithm. The analyses presented in sections 3 and 4 include the observed reflectivity fields.

A simplified HID lookup table based on reflectivity and temperature was created using 79 S-Pol RHI scans from eight precipitation events during NAME. To create the simplified HID algorithm, a basic template for the lookup table was first produced based on general reflectivity– and temperature–hydrometeor type relationships for tropical rainfall given by May and Keenan (2005, see their Table 1). The template was adjusted to best represent the NAME S-Pol RHI fuzzy logic-based HID dataset on a gate-by-gate basis. At each gate in an S-Pol RHI scan, there was a corresponding value of reflectivity

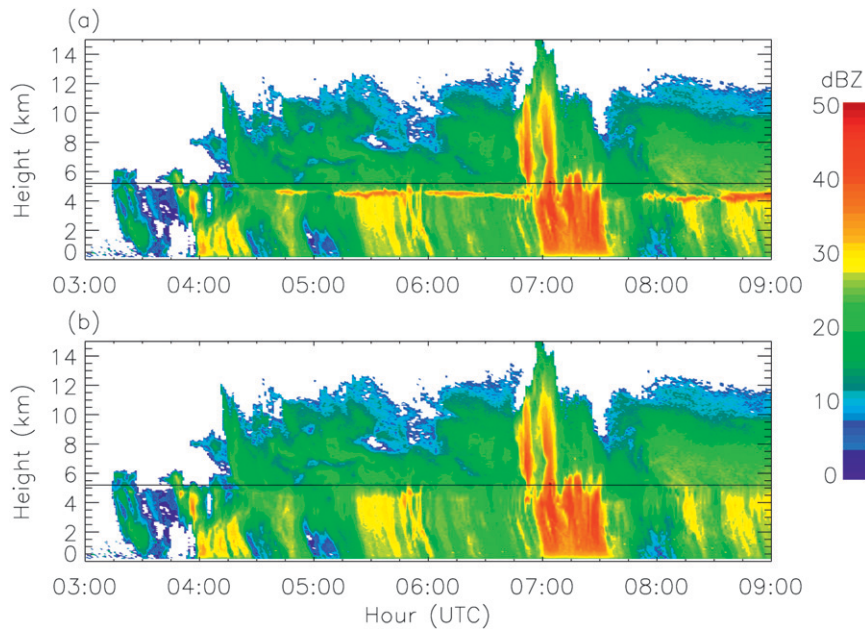


FIG. 3. Time vs height contour plots from 0300 to 0900 UTC 13 Aug 2004 of (a) calibrated S-band profiler equivalent reflectivity and (b) brightband linear-corrected reflectivity used in the simplified HID algorithm. The 0°C line is plotted in black.

and fuzzy logic based HID. Each gate was also assigned a temperature value based on the gate's height above sea level, using a proximate sounding from Mazatlán, Mexico, that was taken within 5 h of the RHI scan. One case (6 RHIs), however, made use of a sounding that was taken within 10 h of the RHI scans, as the nearest 1200 UTC sounding was unavailable. An HID based only on reflectivity and temperature was then calculated at every gate using the lookup table. The reflectivity and temperature boundaries of the lookup table were adjusted to maximize the match between the profiler HID and the S-Pol HID over the profiler site. The final simplified HID lookup table is given in Fig. 4. Identifiable hydrometeor species include, drizzle, rain, dry snow, wet snow (i.e., the melting layer), low-density (dry) graupel, high-density (wet) graupel, and hail. The lower bulk density of dry graupel compared to wet graupel yields a lower dielectric factor for dry graupel. As a result, high-density graupel tends to be associated with higher reflectivity values than that of low-density graupel. In the case of NAME, the reflectivity threshold (at the S band) for discriminating high- and low-density graupel was 41 dBZ (Fig. 4). The performance of the simplified HID algorithm relative to the S-Pol fuzzy logic-based scheme for every hydrometeor type is presented in Table 1. All statistics are based on gate-by-gate comparisons between the profiler and S-Pol data. The algorithm proved effective, matching the S-Pol fuzzy logic output just over 91% of the time (in a gate-by-gate sense). The largest

differences in the profiler-based algorithm and that of the fuzzy logic-based S-Pol dataset occurred in the classifications of wet snow, high-density graupel, and hail, where the lookup table matched the polarimetric-based output 69.9%, 71.6%, and 65.1% of the time, respectively (Table 1). The polarimetric variables more accurately classified various hydrometeor types within the melting layer while the simplified algorithm simply treated the layer as wet snow or high-reflectivity graupel and hail. It should be noted that the simplified HID algorithm

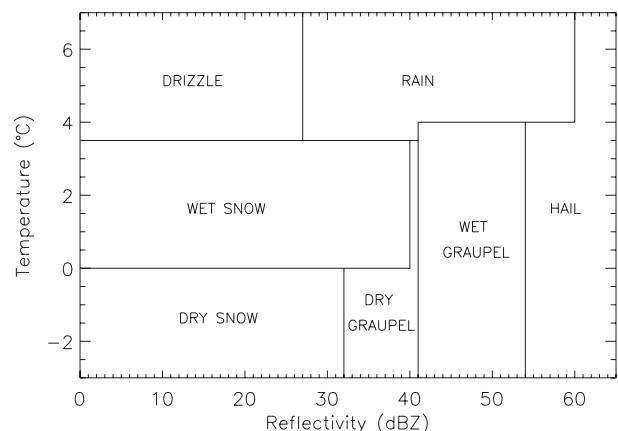


FIG. 4. Lookup table for NAME hydrometeor identification based on S-Pol reflectivity and temperature. Note that the same HID-reflectivity relationship exists for all temperatures greater than 4°C. The same is true for temperatures <0°C.

TABLE 1. Statistics on the performance of the simplified HID lookup table based on S-band reflectivity and temperature relative to the S-Pol fuzzy logic-based approach. Specific hydrometeor types include drizzle (DZ), rain (RN), dry snow (DS), wet snow (WS), dry graupel (DG), wet graupel (WG), and hail (H). The statistics for the DZ category are based on 201 604 gates, RN on 170 597 gates, DS on 378 295 gates, WS on 29 830 gates, DG on 18 796 gates, WG on 10 982 gates, and H on 364 gates.

S-Pol date	No. of RHIs	HID accuracy (%)	DZ (%)	RN (%)	DS (%)	WS (%)	DG (%)	WG (%)	H (%)
All cases	79	91.4	92.1	85.2	96.1	69.9	85.1	71.6	65.1
22 Jul	6	93.2	86.6	90.8	95.9	52.3	83.8	11.8	—
31 Jul	4	94.7	84.4	91.2	98.9	69.7	93.0	49.7	—
3 Aug	16	94.7	92.7	91.4	97.8	74.7	93.4	74.4	—
5 Aug	5	92.9	85.8	89.0	99.5	76.7	66.5	71.3	—
6 Aug	1	91.1	92.3	70.3	95.3	72.8	78.9	70.9	90.9
8 Aug	10	89.9	91.5	84.3	95.4	62.1	76.9	77.9	64.3
9 Aug	31	89.5	92.8	82.3	93.9	72.1	73.8	68.4	—
11 Aug	6	92.2	94.9	83.6	96.3	50.4	84.2	65.3	—
All cases: No WS	79	93.4	95.9	90.0	96.3	69.9	86.5	71.8	65.1

matched the S-Pol fuzzy logic output 93.4% of the time (again, in a gate-by-gate sense) when gates within the melting layer were assumed classified correctly by the simplified algorithm. This 2% increase in accuracy was primarily due to the drizzle and rain categories (Table 1). Hail and high-density graupel classifications suffered largely in part due to a lack of observations. From the 810 468 gates from the 79 RHI scans that were used to create the lookup table, only 364 were classified as hail with the S-Pol polarimetric-based HID algorithm and 10 982 as high-density graupel. Conversely, the dry snow and drizzle classifications performed remarkably well largely in part because of the large number of S-Pol classifications (378 295 and 201 604, respectively), most of which existed in easily identifiable stratiform regions (not shown).

It was desirable to incorporate vertical air motion estimates into the analyses to assess kinematics of North American monsoon convection. Vertical air motion can be estimated using a variety of methods, including both single- and dual-Doppler scanning radar techniques. Low-frequency vertically pointing profilers can also be exploited for this purpose (50, 449, and 915 MHz). However, single-Doppler scanning techniques are generally restricted to two-dimensional flows and NAME instrumentation did not provide for dual-Doppler scanning. Furthermore, 50-MHz profilers were not available during NAME. Williams et al. (2007) estimated vertical air motions during NAME combining 449-MHz profiler measurements with those from the S-band profiler. However, these estimates were only made within regions of stratiform rainfall below the melting layer ( $\sim 4$  km). This study attempted to estimate vertical air motion from the entire S-band profiler dataset making use of the fact that at the S band, the measured Doppler velocity spectrum is the convolution of the fall velocity spectra associated with the hydrometeor size distribution and the vertical air

motion spectrum (Williams et al. 1995). An attempt was made to isolate the vertical air motions from the hydrometeor motions by removing bulk hydrometeor terminal fall velocities from the Doppler velocity measurements. While the vertical air motion estimates appeared reasonable they were not used in this study, as there was no method to verify their accuracy (error) above the melting level or in convective regions. Instead, this study focused on the reflectivity-weighted Doppler velocity data sampled by the profiler (sum of bulk particle fall speed and vertical air motion). Note that this study used the meteorological sign convention that positive Doppler velocities indicate motion away from the radar, meaning that positive (negative) Doppler velocities observed by the profiler represent net upward (downward) motions.

### 3. Vertical structure of convective precipitation events

A number of studies have shown that during the North American monsoon, precipitation develops almost ubiquitously along the high terrain of the SMO in the early afternoon and subsequently propagates toward the coast at lower elevations (Gochis et al. 2007; Nesbitt et al. 2008; Rowe et al. 2008). Lang et al. (2007) further defined various precipitation regimes during NAME based on the propagation characteristics of convection. Regime A corresponded to propagation of cross-coast systems. Regime B corresponded to along-coast propagation. Regime AB was defined when both regimes A and B occurred simultaneously. Periods when none of the three identified regimes occurred were referred to as undisturbed periods.

This study examined the five most intense convective passages over the S-band profiler during NAME, three of which are presented here. The cases were analyzed to better understand the details in the vertical structure of

TABLE 2. Case information on the three rainfall events presented in this study.

Event date	Time of passage (UTC)	Regime	Rainfall (mm)	Mazatlán sounding for HID
3 Aug	1700–2100	AB	32.5	1600 UTC 3 Aug
5–6 Aug	2000–0500	AB	11.9	0000 UTC 6 Aug
13 Aug	0315–0900	A	35.3	0000 UTC 13 Aug

North American monsoon precipitation as well as to test the robustness of the simplified HID algorithm. Cases were chosen based on their maximum intensity (maximum Doppler velocities), vertical extent, and time length of convective passages. Case information on the selected rain events is given in Table 2, including time of passage, Lang et al. (2007) regime classification, rainfall totals, and the soundings used for profiler-based HID.

#### a. 3 August 2004, regime A

Intense convective rain characterized the 3 August precipitation event. An MCS organized along the west coast of central Mexico near 1200 UTC. The system continued to strengthen as it propagated northward along the coast, reaching the profiler site at approximately 1800 UTC. The period was characterized by regime A as described by Lang et al. (2007). The onsite rain gauge recorded nearly 33 mm of rain during the cell's passage. Figure 5 shows S-Pol reflectivity as the precipitation moved over the profiler site. The southwest–northeast-oriented convective line spanned nearly 100 km as it moved north, along the coast. As the system approached the profiler site, the profiler experienced mixed stratiform–convective rainfall. The core of the convection moved over the site around 1830 UTC. By 1901 UTC, the main convection had passed the profiler site and began to dissipate leaving only mixed stratiform–convective rain behind the main convective line. Figure 6 displays the vertical structure of precipitation as recorded by the NOAA S-band profiler. A mixture of convective- and stratiform-like elements passed over the profiler from 1700 to 1800 UTC. The precipitation-type algorithm had difficulty categorizing the precipitation profiles, classifying mixed stratiform–convective precipitation from 1700 to 1725 UTC, then convective precipitation from 1725 to 1800 UTC with brief stratiform periods at 1730 and 1750 UTC (Fig. 6a). This passage was also characterized by low reflectivity aloft and dry snow above 5 km. Convective elements were shallow, composed of vertical streaks of moderate to high reflectivity embedded within reflectivity less than 30 dBZ (Fig. 6a), suggestive of shallow convection embedded within stratiform rain. The profiler identified HID profiles with primarily rain below the melting layer, dry snow aloft, and the melting layer identified as wet snow. The two periods identified as stratiform were associated with light drizzle (Fig. 6c). S-Pol suggested

a similar HID structure, but with poorer vertical resolution (Fig. 6d). S-Pol failed to pick up the weak precipitation streak observed by the profiler near 1700 UTC and only identified drizzle at 1715 UTC. The associated Doppler velocity contained a trimodal vertical structure with values between 0 and  $1 \text{ m s}^{-1}$  associated with weak ascent above 7 km, velocities between  $-2.5$  and  $-5 \text{ m s}^{-1}$  from 4.5 to 7 km, and velocities less than  $-5 \text{ m s}^{-1}$  below the melting level (Fig. 6b) associated with rain-cooled downdrafts. The weak updrafts observed aloft during the mixed stratiform–convective period were consistent with the fact that mixed stratiform–convective precipitation often contains turbulent motions above the melting layer (Williams et al. 1995). Convection first appeared over the profiler near the surface with reflectivity around 38 dBZ at 1800 UTC. This marked the passage of the main convective line. Convective precipitation moved over the profiler from approximately 1800 to 1900 UTC, characterized by reflectivity greater than 40 dBZ and heavy rain. A low-level (just below 4 km) updraft with Doppler velocities of  $2 \text{ m s}^{-1}$  was present from 1755 to 1805 UTC. Noting that raindrop fall speeds are on the order of  $7 \text{ m s}^{-1}$  (Joss and Waldvogel 1970), the observed Doppler velocities suggest that this low-level convection exhibited updraft speeds  $\sim 9 \text{ m s}^{-1}$ . A strong upper-level downdraft with Doppler velocities near  $-10 \text{ m s}^{-1}$  persisted from 1805 to 1820 UTC, and steadily decreased in height from 13 to 5 km during this time. Similar Doppler velocity magnitudes have been recorded by profiling radars when observing convective updrafts and downdrafts over northern Australia (Cifelli and Rutledge 1994; Ecklund et al. 1999; May and Keenan 2005). At 1820 UTC, both a mid- and upper-level updraft with peak Doppler velocities greater than  $3.5 \text{ m s}^{-1}$  became apparent along with the presence of a significant graupel region extending above the freezing level. The upper-level updraft increased in height with time up to 14 km, suggesting a tilted updraft. Just after 1830 UTC the updraft region was replaced by Doppler velocities less than  $-5 \text{ m s}^{-1}$  at midlevels. By 1840 UTC, these downward velocities extended to all levels and persisted until 1900 UTC. The exception was a small region of updraft between 6 and 8 km at 1845 UTC. Velocities less than  $-10 \text{ m s}^{-1}$  were evident in the lowest 6 km. This was likely a region where graupel was falling within the downdraft, after being ejected from the adjacent updraft

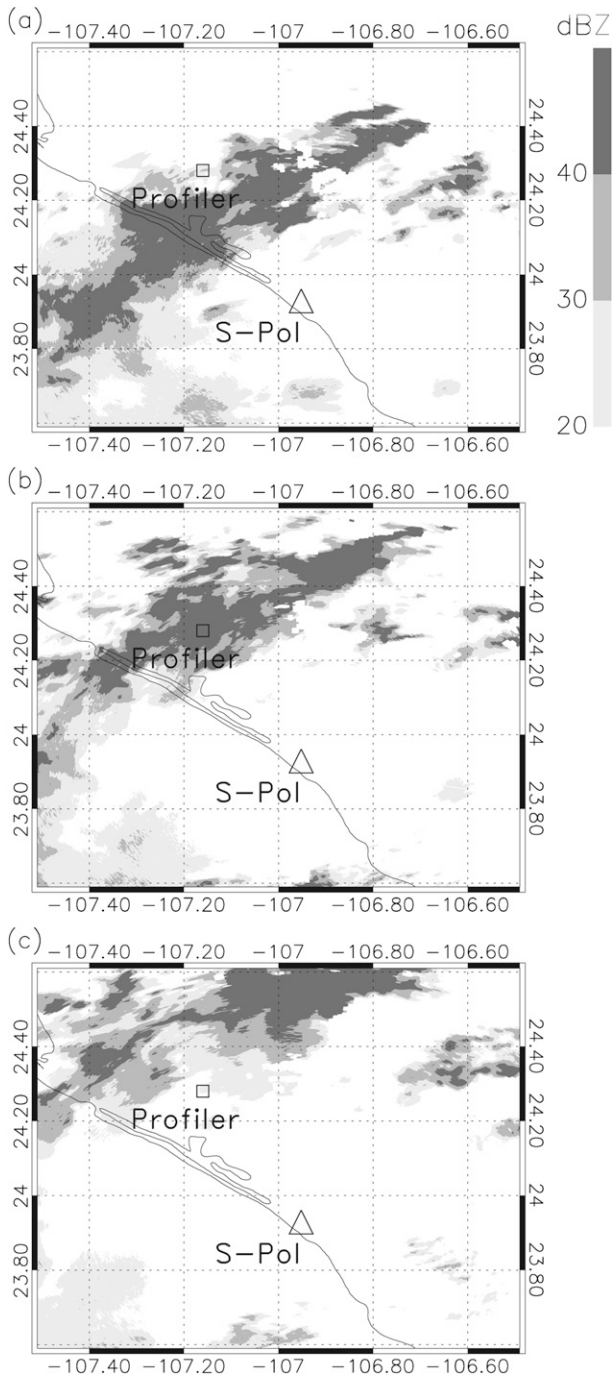


FIG. 5. PPIs at 1.3° elevation angle over the NAME tier-I region at (a) 1801, (b) 1831, and (c) 1901 UTC 3 Aug. Lines of longitude and latitude are in degrees.

above. This is supported by the S-Pol HID analyses. Just after 1815 UTC, low-density graupel was only identified at 6 km. However, the maximum height of graupel extent increased with time, reaching 13 km by 1845 UTC. It was at the time of the downdraft passage observed by

the profiler when high-density graupel was first observed by the S-Pol below the melting level. However, this highlighted a significant difference between the profiler- and S-Pol-based HID fields during convection. The S-Pol identified low-density graupel through 13 km while the profiler identified low-density graupel only through 9 km. Both analyses identified high-density graupel within the melting layer between 1830 and 1845 UTC. However, the S-Pol observed a larger region of high-density graupel that extended slightly below the melting layer. It was not possible for the profiler-based estimates to identify high-density graupel in this region because of the temperature constraints imposed by the simplified HID algorithm, which only allowed high-density graupel to be classified at temperatures colder than 4°C (Fig. 4).

Figure 7 displays an S-Pol RHI cross section over the profiler site at 1835 UTC. The profiler site is located at 44.42-km range. A convective region with reflectivity greater than 40 dBZ existed from 34- to 60-km range from the S-Pol radar (Fig. 7a). At this time, the region of greatest storm vertical extent (15 km) as well as graupel vertical extent (12 km) was situated over the profiler, near the 44-km range. High-density graupel over the profiler was situated between 4 and 6 km with primarily low-density graupel aloft (Fig. 7b). The maximum reflectivity over the profiler exceeded 50 dBZ, though higher reflectivity existed at 4 km immediately north and south. The profiler site experienced heavy rainfall at this time, implied by the profiler and S-Pol HID fields and verified by the onsite rain gauge. The S-Pol Doppler velocity field showed low- to midlevel southerly flow near 10 m s<sup>-1</sup> that decreased in height with range. Just above this region, flow toward the radar existed at midlevels as great as 10 m s<sup>-1</sup> over the profiler site (Fig. 7c). This flow also decreased in height with range. Storm top divergence was evident at a range of 42 km, just southeast (lesser range) of the profiler location. This vertical structure suggested the presence of an updraft at mid- to upper levels with a downdraft just below it over the profiler location, which led to graupel production and fallout, consistent with the profiler analyses. However, S-Pol reflectivity values greater than 30 dBZ extended to 12 km over the profiler at 1835 UTC. This was inconsistent with corresponding S-band profiler measurements, which only showed maximum reflectivity values near 27 dBZ at this altitude (Fig. 6a). While likely that these reflectivity inconsistencies were at least partly due to differences in spatial sampling between the two instrument platforms (Cifelli et al. 1996; Gage et al. 2000), it is possible that profiler reflectivity calibration or profiler attenuation in deep convection may have played a contributing role. The S-band profiler reflectivity was calibrated to that of S-Pol using observations below the radar bright band, assuming that raindrops have similar

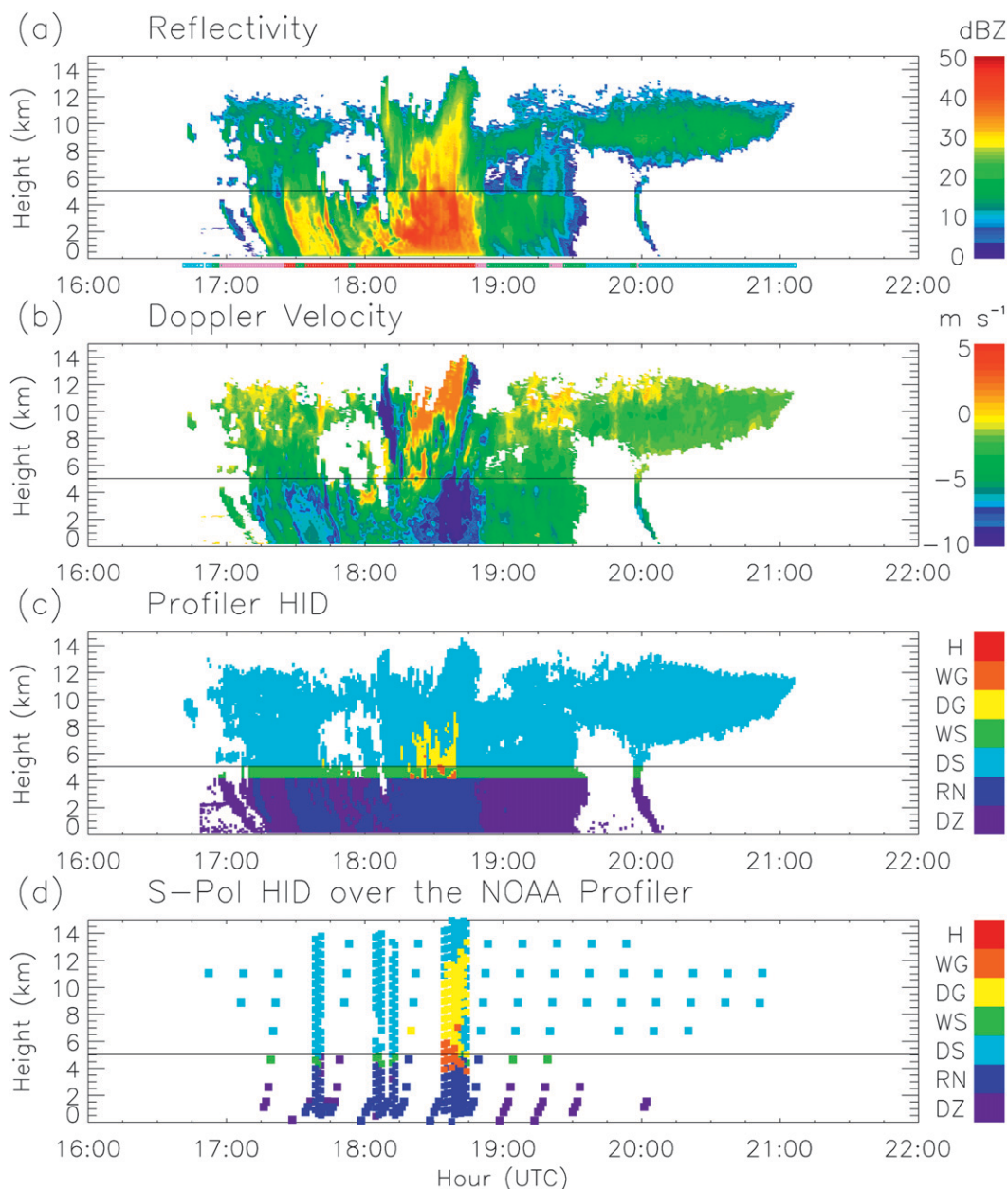


FIG. 6. Time vs height contour plots of the (a) equivalent reflectivity factor, (b) Doppler velocity, and (c) HID for the 3 Aug 2004 rainfall event from the S-band profiler from 1600 to 2200 UTC. (d) The nearest pixel S-Pol HID over the profiler. HID is contoured for drizzle (DZ), rain (RN), dry snow (DS), wet snow (WS), low-density (dry) graupel (DG), high-density (wet) graupel (WG), and hail (H). Positive (negative) velocities indicate upward (downward) motion in (b). The color code below (a) represents the precipitation-type classification of each profile: green is stratiform, red is convective, pink is mixed stratiform-convective, and light blue is the upper level cirrus. 0°C lines are overlaid in black near 5 km.

radar cross sections when viewed at horizontal and vertical incidence angles (Williams et al. 2007). In ice regions, however, wind shear and asymmetric particle shapes can yield different radar cross sections when viewed at horizontal versus vertical incidence angles (at horizontal polarization). This may attribute to differences in the

observed reflectivity between the S-Pol and the profiler. It is also possible, though unlikely, that the higher S-Pol reflectivity values resulted from sidelobe illumination of the bright band (Campos et al. 2008). Isolating the exact cause(s) for these reflectivity differences is admittedly difficult.

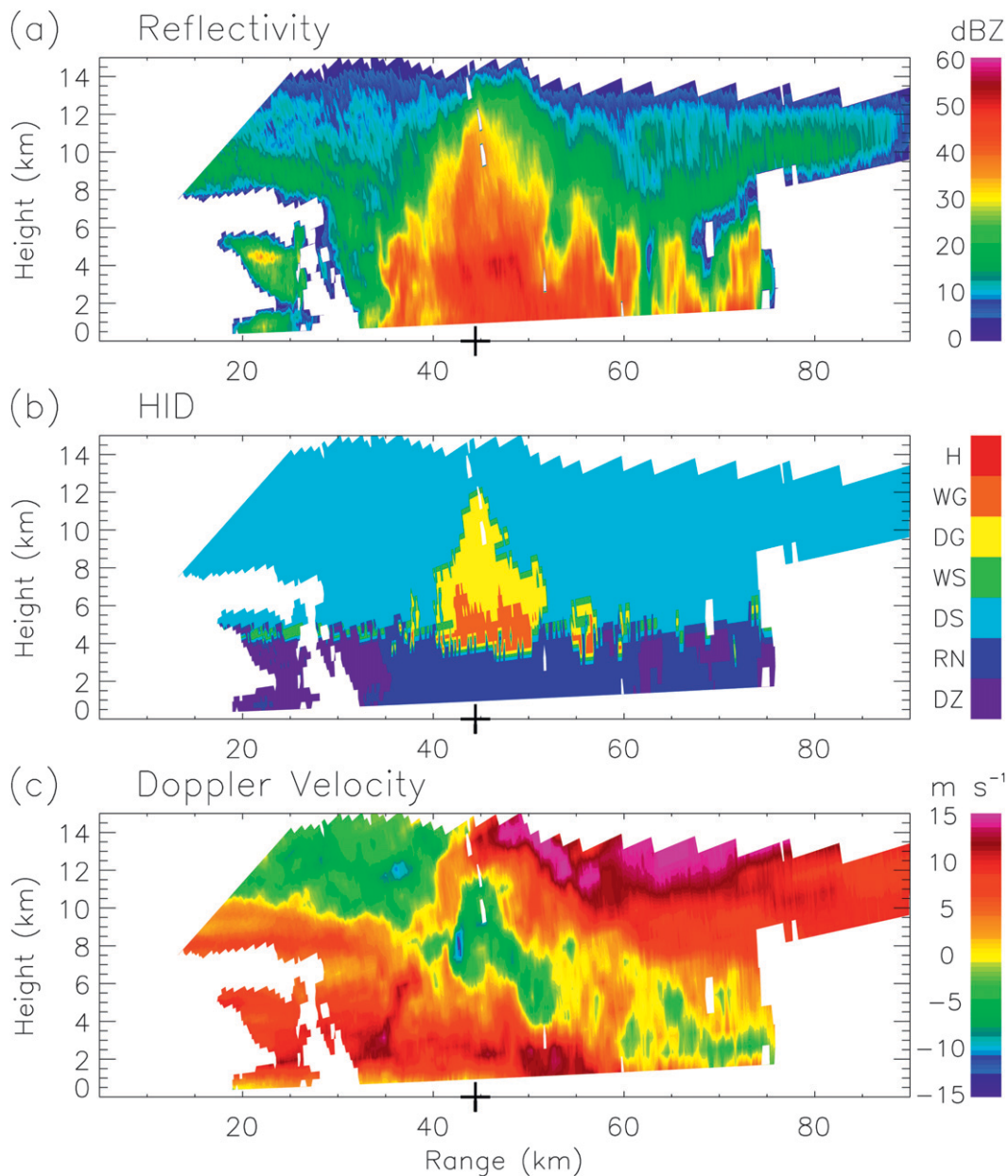


FIG. 7. S-Pol RHI taken over the NOAA profiler site ( $331^{\circ}$  azimuth) at 1835 UTC 3 Aug 2004. The radar variables displayed include (a) reflectivity, (b) HID, and (c) mean Doppler velocity. The range of the profiler site relative to S-Pol is marked with a black cross in (a)–(c) (44.42 km). HID is contoured for the same hydrometeor types as in Fig. 6.

The profiler site experienced mainly stratiform precipitation from 1850 to 1930 UTC. However, brief mixed stratiform convective precipitation passed from 1905 to 1920 UTC. The same trimodal structure in Doppler velocity that occurred prior to the convection was evident throughout this stratiform regime, though Doppler velocities below 4 km only reached  $-5 \text{ m s}^{-1}$  as opposed to  $-10 \text{ m s}^{-1}$  observed prior to 1900 UTC. S-Pol HID was identical to that of the profiler during this time, though at

poorer resolution. After 1930 UTC, the profiler measured primarily upper level storm outflow, except for a brief precipitation passage at 2000 UTC. Both the S-Pol and profiler HID fields identified drizzle at low levels during this passage.

#### *b. 5–6 August 2004, regime AB*

The 5–6 August MCS event occurred during the evening hours and consisted of two separate cells passing the

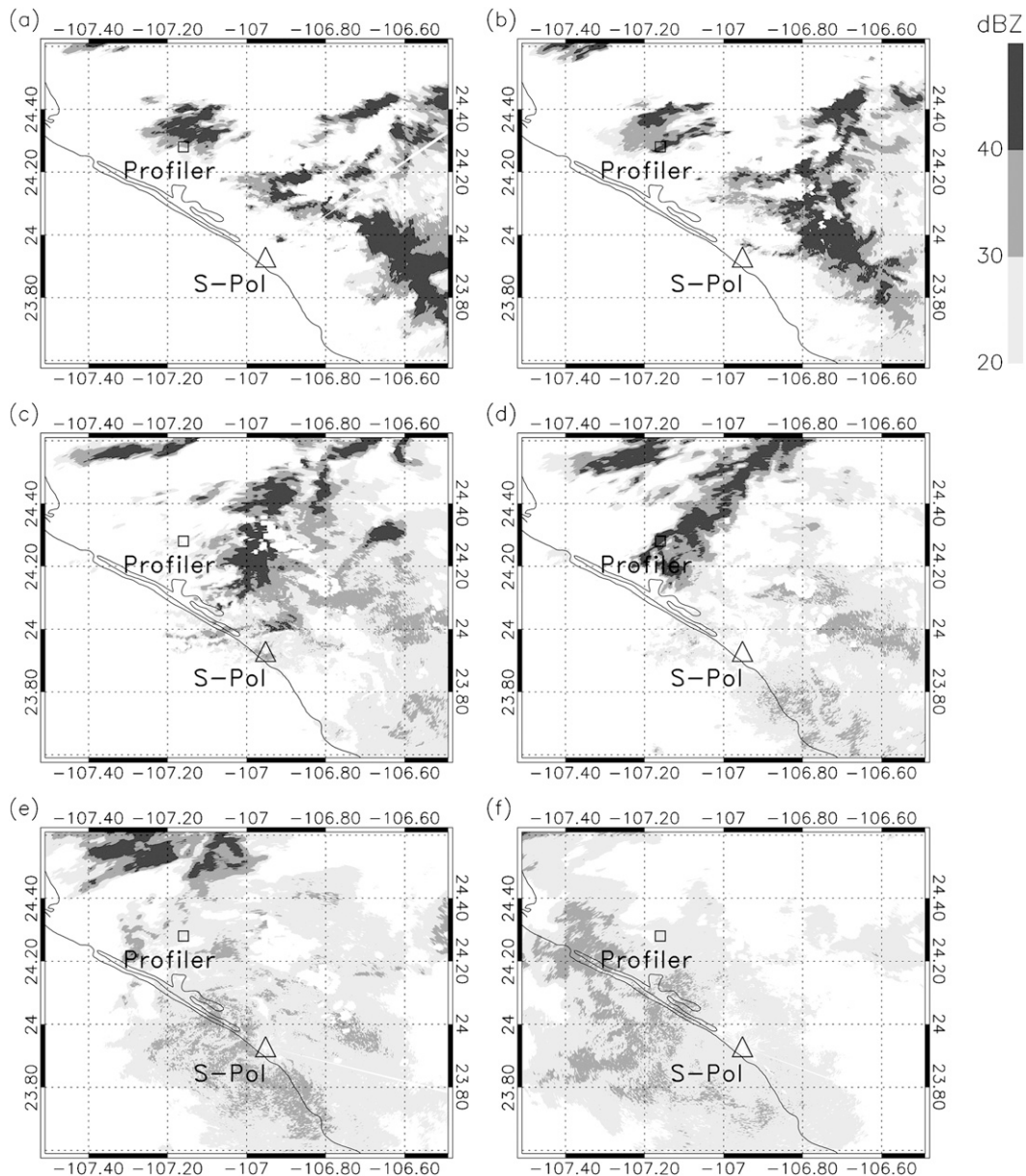


FIG. 8. As in Fig. 5, but for (a) 2131, (b) 2146, (c) 2231, (d) 2301, and (e) 2331 UTC 5 Aug 2004 and (f) 0016 UTC 6 Aug 2004.

profiler site in succession, yielding nearly 12 mm of total accumulated rainfall between 2130 UTC 5 August and 0220 UTC 6 August. Figure 8 depicts the evolution of S-Pol reflectivity over the profiler. As characteristic of regime AB identified by Lang et al. (2007), both along-coast and cross-coast orientation of developing convection was evident at 2131 UTC 5 August. At 2146 UTC the western edge of an isolated convective cell passed directly over the profiler. This cell, oriented southwest to northeast, propagated to the northwest. After the passage of the isolated cell, the profiler site experienced

scattered convection and mixed stratiform–convective rain as the overall convective system continued to organize. At 2301 UTC, the southwest portion of a northeast–southwest-oriented convective line spanning 90 km moved over the profiler. The line weakened as it passed the site to the north at 2331 UTC, and only widespread stratiform rain remained along the coast by 0016 UTC 6 August. Figure 9 displays the vertical structure of convection recorded by the S-band profiler. The profiler and S-Pol identified the passage of a small mixed stratiform–convective cell at low levels near 2000 UTC. The first

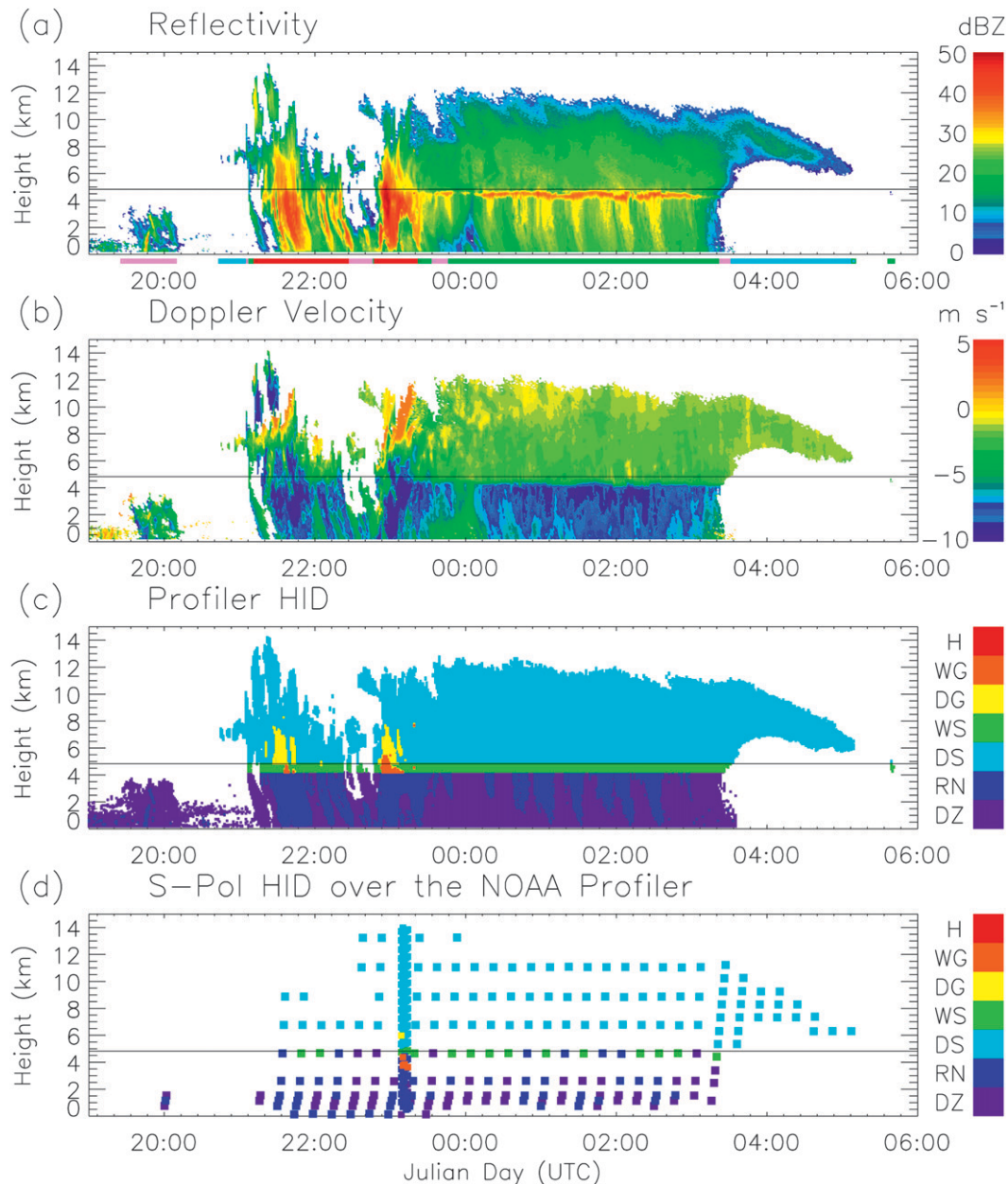


FIG. 9. As in Fig. 6, but from 1900 UTC 5 Aug 2004 to 0600 UTC 6 Aug 2004.

convective cell began to move over the profiler at roughly 2135 UTC with reflectivity greater than 35 dBZ extending to 8 km (Fig. 9a). Doppler velocities at this time were around  $-10 \text{ m s}^{-1}$  above 9 km, as low as  $-8 \text{ m s}^{-1}$  below 6 km, and updrafts with Doppler velocities as great as  $3 \text{ m s}^{-1}$  were observed between 6 and 10 km that increased in altitude with time, suggestive of another tilted updraft (Fig. 10b). Both the profiler- and S-Pol-based HID indicated the presence of rain with this cell and wet snow within the melting layer (Figs. 9c,d). In this case, the profiler observed measurable reflectivity as high as

14 km (dry snow) while S-Pol showed dry snow only up to 9 km. The profiler also identified a graupel core in this cell extending up to 7.5 km with high-density graupel located in the melting layer. The S-Pol radar did not identify graupel. This is likely due to the fact that at this time, only the edge of the convective cell passed directly over the profiler (Fig. 8b). The profiler observed this cell directly whereas S-Pol, with a pulse volume three times as large as the profiler, observed both the small convective cell and surrounding stratiform rain, yielding lower measured values of reflectivity (not shown). In this case, it appears

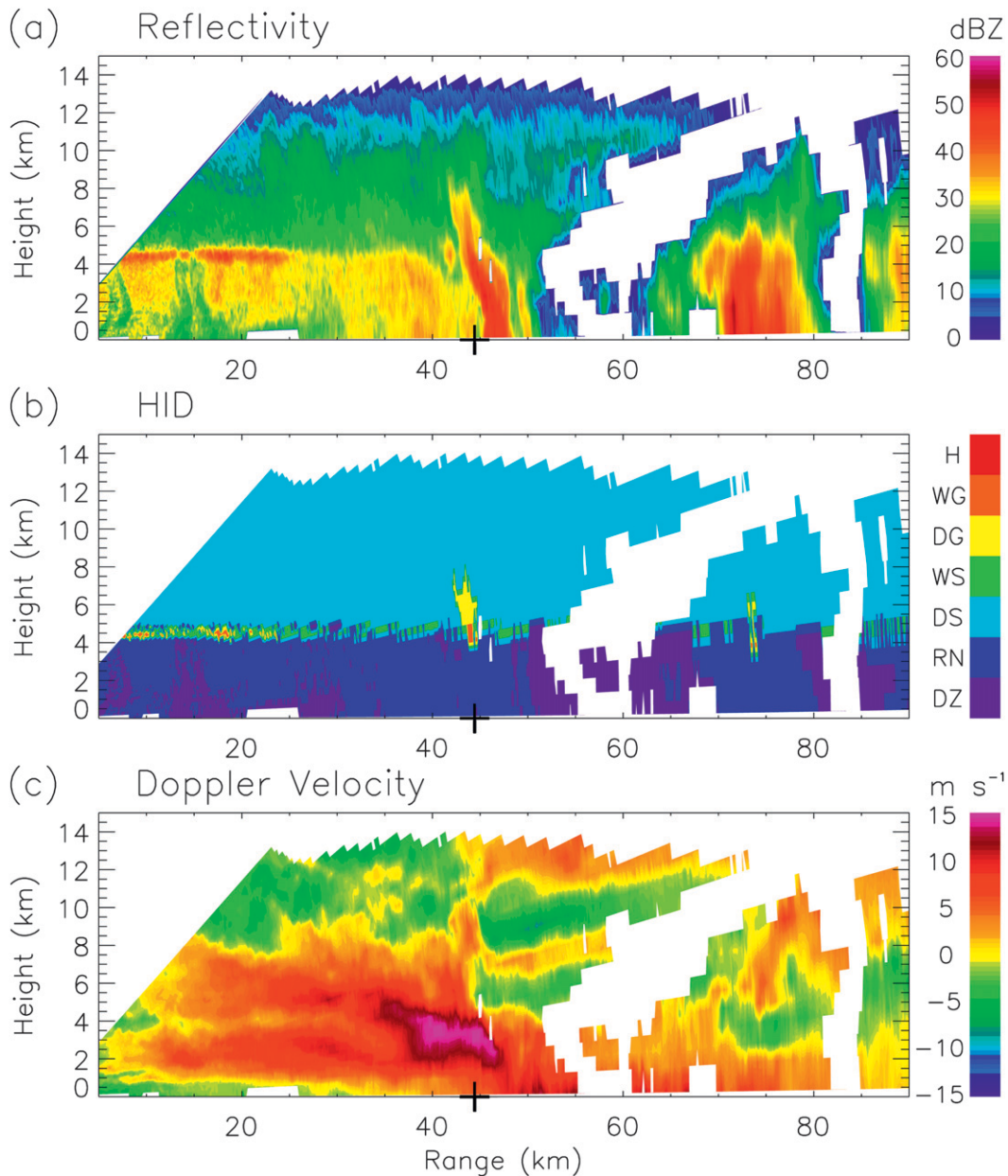


FIG. 10. As in Fig. 7, but for 2308 UTC 5 Aug 2004.

that the NOAA S-band profiler provided for more precise HID over the site than the S-Pol.

As the first convective cell advected away from the profiler site, the profiler recorded multiple convective streaks between 2200 and 2245 UTC. These streaks were associated with reflectivity greater than 38 dBZ, lower Doppler velocities than the surrounding precipitation ( $-7$  to  $-8$   $\text{m s}^{-1}$ ), likely associated with downdrafts, and Doppler velocities that ranged from  $-1$  to  $1$   $\text{m s}^{-1}$  above 5 km. The convective streaks were of lower vertical extent (reaching 7 km) than the convective cell that

passed previously. Profiler and S-Pol HID compared favorably at this time, though the profiler identified more rain than S-Pol. The southwest portion of a well-organized convective line passed over the profiler from 2300 to 2335 UTC (Fig. 8d). The profiler observed reflectivity as large as 50 dBZ between 3 and 5 km with Doppler velocities as low as  $-10$   $\text{m s}^{-1}$  below 6 km and an updraft that increased in height with time containing velocities as high as  $3.5$   $\text{m s}^{-1}$  above 6 km, likely indicating an updraft–downdraft interface located near 6 km. Profiler and S-Pol HID compared well during the

passage of this cell, showing rain, high-density graupel between 4 and 5 km, low-density graupel near 6 km, and dry snow aloft. The profiler identified a larger region of low-density graupel. S-Pol identified high-density graupel just below the melting layer and dry snow through 14 km while the profiler data only reached 12 km, again likely due to reasons discussed in previous sections.

Figure 10 displays an S-Pol RHI scan over the profiler site at 2308 UTC 5 August. The main convection was organized as a leading convective line with trailing stratiform precipitation, oriented primarily west to east (convection only spans 5 km in the north–south orientation of the RHI), with a transition zone of mixed stratiform–convective rain between the ranges of 30 and 40 km and a well-defined trailing stratiform region seen at ranges less than 30 km with a sharp bright band at 4.5 km (Fig. 10a). Storm top divergence was directly over the profiler site at this time. Outbound flow ( $15 \text{ m s}^{-1}$ ) was evident below 5 km with inbound flow immediately above (Fig. 10c). This signature was consistent with the profiler observations, which indicated an updraft–downdraft boundary near 6 km (Fig. 9b). The HID field showed that the profiler was located just north of the main convective core at this time, with low-density graupel reaching 8 km (Fig. 10b). This also supports the profiler-based HID observations within this convective line.

The convective line was followed by a brief passage of mixed stratiform/convective precipitation starting at 2345 UTC, and then transitioned to a well-defined trailing stratiform region through 0330 UTC (Fig. 9a). This was also evident in Fig. 10a. Once the precipitation over the profiler became stratiform based just before 0000 UTC, two features in the melting layer became apparent, both consistent with the findings of Williams et al. (1995) and White et al. (2002, 2003). A bright band was clearly visible in the reflectivity profiles with a sharp transition from reflectivity near 25–30 dBZ to values greater than 37 dBZ. The Doppler velocity gradient sharpened significantly from values near  $-2 \text{ m s}^{-1}$  just above the freezing level to values exceeding  $-8 \text{ m s}^{-1}$  just below it. This intensification was due to the transition from aggregate snow falling at  $1\text{--}2 \text{ m s}^{-1}$  above the freezing level to raindrops falling at  $6\text{--}8 \text{ m s}^{-1}$  below (Battan 1973). The profiler HID was consistent with that of the S-Pol radar, identifying dry snow aloft, wet snow within the melting layer, and drizzle below 4 km that contained embedded pockets of rain. As in previous cases, S-Pol did not identify the wet snow within the melting layer as consistently as the profiler.

#### c. 13 August 2004, regime AB

The 13 August rainfall event was characterized by a nocturnal MCS that produced widespread stratiform

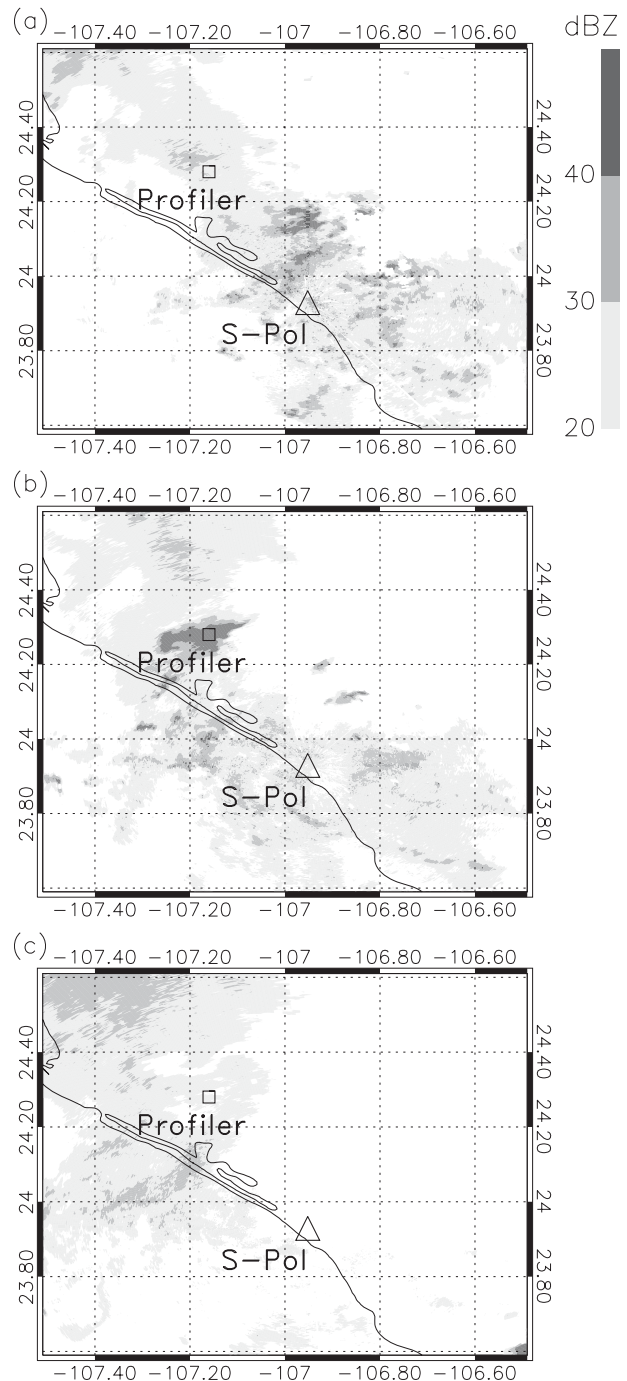


FIG. 11. As in Fig. 5, but at (a) 0601, (b) 0716, and (c) 0816 UTC 13 Aug 2004.

precipitation with multiple embedded convective cells. Convection began to organize along the southwest Mexican coast near 0145 UTC. By 0345 UTC organization had led to multiple MCSs. The northern MCS passed over the profiler site just after 0645 UTC. Figure 11 displays the time evolution of S-Pol reflectivity as the precipitation

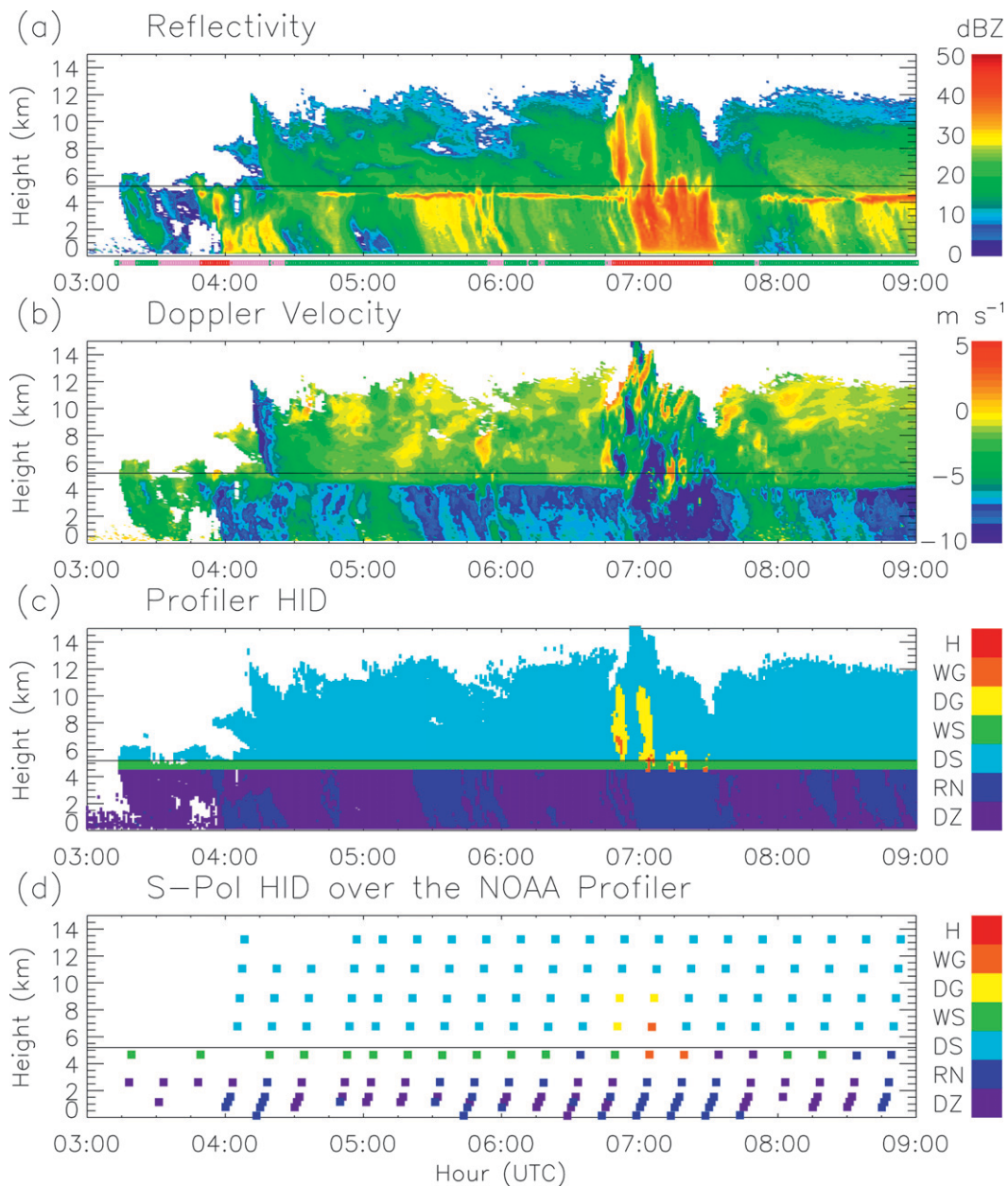


FIG. 12. As in Fig. 6, but from 0300 to 0900 UTC 13 Aug 2004.

moved over the profiler site. Developing convection approached from the southeast. Convection was aligned east–west while the surrounding stratiform region was oriented along the coast in a northwest–southeast orientation. Lang et al. (2007) characterized this event as regime AB. The convective elements organized into a single cell and reached the profiler by 0716 UTC. By 0816 UTC, convection dissipated as it passed the profiler site, leaving behind widespread stratiform rain along the coastline. The southwestern portion of a line of convective cells reached the profiler near 0347 UTC, and

new convection formed north of S-Pol around 0547 UTC (not shown). From approximately 0645 to 0730 UTC, a mature convective cell passed over the profiler site (Fig. 11) and produced 26 mm of rainfall. This was followed by widespread stratiform precipitation throughout the morning hours (not shown). The on-site rain gauge recorded 9.4 mm of stratiform rainfall between 0300 and 0900 UTC. Figure 12 depicts the vertical structure of precipitation with time over the S-band profiler. Low-level mixed stratiform/convective precipitation, classified as drizzle by the profiler and S-Pol, first reached the

site around 0315 UTC, accompanied by modest reflectivity (Fig. 12a;  $<25$  dBZ) and Doppler velocities near  $-3$   $\text{m s}^{-1}$  (Fig. 12b). By 0350 UTC, this progressed into stronger shallow convection, with reflectivity greater than 35 dBZ in the lowest 5 km. This convection contained an updraft with Doppler velocities near  $2$   $\text{m s}^{-1}$  at 5 km and velocities near  $-7$   $\text{m s}^{-1}$  at low levels, associated with rain. This passing cell was part of a larger system characterized by multiple cells embedded in stratiform rain. Around 0415 UTC, an upper-level downdraft was detected with maximum Doppler velocities of  $-10$   $\text{m s}^{-1}$  observed. This downdraft was present for 15 min in the profiler time series and was immediately followed by a brief updraft with Doppler velocities of  $3$   $\text{m s}^{-1}$  near 10 km. The next 1.5 h were characterized primarily by stratiform precipitation with a short convective passage near 0550 UTC. As in previous events, the stratiform precipitation was characterized by a well-defined bright band and strong Doppler velocity gradient. There was a reduction in the radar bright band just after 0630 UTC, which may have been due to enhanced subsidence in the region. This can only be inferred, as downward Doppler velocities do not necessarily identify downdrafts (see section 2 regarding Doppler velocity with respect to air and hydrometeor motion). The profiler and S-Pol HID fields were nearly identical from 0315 to 1630 UTC, identifying a consistent wet snow melting layer with dry snow aloft and drizzle below with embedded regions of rain, associated with reflectivity greater than 27 dBZ (Figs. 12c,d).

A 15-km-wide convective cell passed directly over the profiler site from 0645 to 0730 UTC (Fig. 11b), with reflectivity greater than 48 dBZ and attendant strong updraft and downdraft signatures (Figs. 12a,b). Doppler velocity revealed alternating fingers of updrafts and downdrafts above 5 km throughout the cell's passing (3.5 and  $-10$   $\text{m s}^{-1}$ , respectively). While a single convective cell is evident in the S-Pol PPIs (Fig. 11b), the Doppler velocity pattern suggests a multicell passage. At 0650 UTC, the profiler observed an upper-level region (5–11 km) of reflectivity greater than 40 dBZ associated with low- and high-density graupel near 6 km (Fig. 12c). These profiles were indicative of graupel particles falling through updrafts too weak to support them, possibly after they had been ejected from stronger updrafts aloft. S-Pol HID analyses were generally consistent with those of the profiler at this time (Fig. 12d). However, the S-Pol did not identify any high-density graupel in this column. A similar feature was evident just after 0700 UTC but here the graupel region extended to the base of the melting layer and reflectivity greater than 40 dBZ extended from 10 km down to the surface, indicative of heavy precipitation. The profiler and S-Pol HID identified

rain during this passage and graupel that reached 10 km. However, profiler HID identified low-density graupel above the melting layer with high-density graupel below 5 km and a small presence of hail at 5.5 km. The S-Pol HID identified no hail but observed high-density graupel up to 6 km. This region contained downdrafts between 3 and 7 km with measured Doppler velocities less than  $-9$   $\text{m s}^{-1}$  and was possibly an area where graupel particles moved through the melting layer prior to complete melting. At 0715 UTC, another graupel-dominated region between 4 and 5 km was over the profiler. The S-Pol identified a small patch of high-density graupel in this region. However, this region was associated with an updraft at 5.5 km with Doppler velocities as high as  $4$   $\text{m s}^{-1}$ . Graupel generally falls at speeds between 1 and 3  $\text{m s}^{-1}$  (Locatelli and Hobbs 1974), indicating that this graupel was likely being carried aloft in the storm, suggestive of a graupel production zone with peak updrafts near  $7$   $\text{m s}^{-1}$ . The 45-s temporal resolution of the profiler output was seemingly beneficial in this case as the profiler was able to identify two separate regions of graupel aloft at 0650 and 0700 UTC. The resolution of S-Pol would have suggested that the convective core passed over the profiler continuously from 0650 to 0715 UTC. It would have been useful to analyze the convective cell in two-dimensional space with S-Pol RHI scans. Unfortunately, no such scans were performed over the profiler site during the cell's passage and it was therefore unclear as to what exact hydrometeor types were present. Convection was followed by a mixed stratiform–convective regime until 0750 UTC, apparent as profiles of low reflectivity with no clear radar bright band. All precipitation that followed was stratiform (Fig. 12). The profiler took continuous measurements until approximately 1000 UTC (not shown) when a power outage occurred due to a lightning strike. Profiler and S-Pol HID fields were nearly identical throughout the 13 August rainfall event, with merely slight differences in graupel identification during the convective passages.

#### 4. Profiles of precipitating clouds

Merged profiles of stratiform and convective precipitation during NAME were created from the full S-band profiler dataset (all 23 rain events). In this section these profiles are compared to those from previous field programs in an attempt to determine how the structures of North American monsoon precipitation compare to those in other tropical locations.

##### a. Stratiform

Figure 13 depicts cumulative frequency distributions (CFDs) of reflectivity in stratiform rainfall for NAME

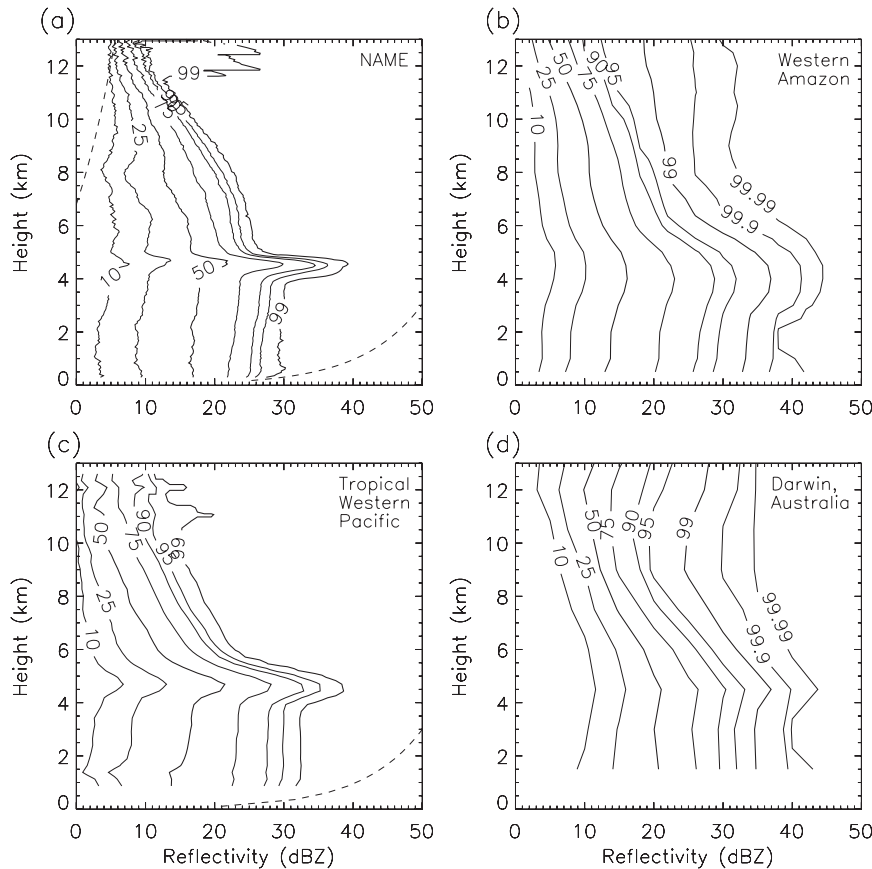


FIG. 13. CFDs of reflectivity in stratiform rainfall for (a) NAME, (b) the western Amazon West regime, (c) the tropical western Pacific, and (d) Darwin, Australia. Profiler saturation is shown as dashed lines. (b) Adapted from Cifelli et al. (2004). (d) Adapted from Steiner et al. (1995).

2004 using the 2875-MHz profiler, the western Amazon West Regime (WR) during January and February of 1999 using S-Pol (Cifelli et al. 2004), the tropical western Pacific during November 1992–February 1993 using the vertical beam of a 915-MHz wind profiler radar that was aboard the ship *R/V Kexue #1* during the Tropical Ocean and Global Atmosphere Coupled Ocean–Atmosphere Response Experiment (TOGA COARE), and Darwin, Australia, during February 1988 using a scanning C-band radar (Steiner et al. 1995). Each study was selected for its respective tropical location. Note that the stratiform CFD associated with the western Amazon East Regime (ER; Cifelli et al. 2004, not shown) is nearly identical to that of the WR. The NAME distribution (Fig. 13a) shows reflectivity slightly increasing with height below 4 km. A significant bright band is evident at 4.5 km where reflectivity sharply increases by 3–4 dBZ and immediately drops by the same amount by 5 km. Reflectivity then gradually decreases with height above the melting layer. For instance, the 50% contour in the NAME distribution is near 17 dBZ at low levels, increases to 18 dBZ by 4 km

and increases to 22 dBZ in the bright band. The reflectivity decreases back to 17 dBZ at 5 km, continues to decrease with height, and reaches 7 dBZ by 12 km. This compares well with the other distributions. However, the NAME distribution shows the weakest precipitation below 4 km, as evident by the 99% contours.

While the various distributions seem to suggest that NAME exhibited a narrower melting layer than the other studies, the result is likely an artifact of the vertical resolution used in the profiles. The vertical resolution of the scanning-radar-based profiles is on the order of a kilometer and the 915-MHz profiler used to create the western Pacific distribution utilized a gate spacing of 495 m. The S-band profiler used during NAME had significantly higher vertical resolution (60 m) than these previous studies and was therefore able to identify the bright band more effectively.

#### b. Convective

CFDs of convective precipitation are displayed in Fig. 14 for the same locations that were previously discussed regarding stratiform precipitation. Note that the data

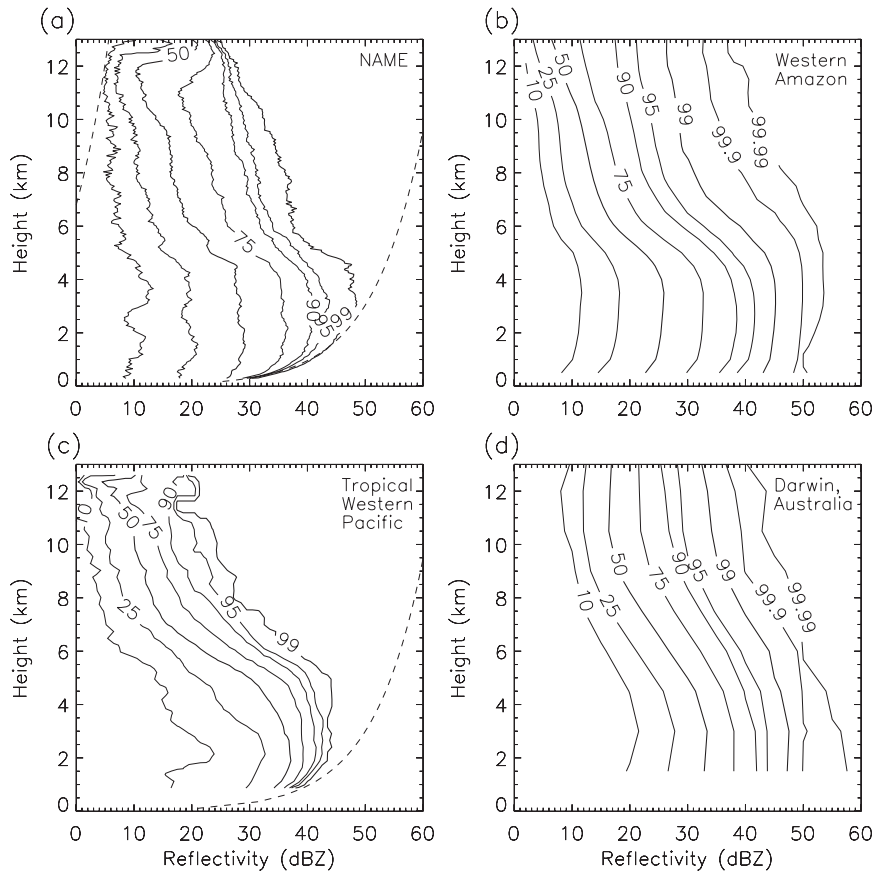


FIG. 14. As in Fig. 13, but for convective precipitation.

used to create the Darwin CFD were collected from both monsoonal and break conditions (Steiner et al. 1995). While separate CFDs of stratiform precipitation for these two regimes may look similar, the CFDs of convective precipitation for each regime would likely appear quite different compared to the net composite shown in Fig. 14d. The NAME distribution (Fig. 14a) shows high reflectivity increasing in magnitude from the surface up to 4 km, decreasing values with height above 5 km, and nearly constant reflectivity with height above 10 km. This structure is primarily visible in the 90%, 95%, and 99% contours but somewhat evident in the 75% contour as well. This general structure is evident in all four profiles (Figs. 14a–d). However, the NAME distribution depicts significant increases in large reflectivity with height in the lowest 2 km (75% contour and above). This is due to the fact that for heavy rainfall at low levels, the energy transmitted back to the vertically pointing profiler radar receiver is greater than the power required to saturate the receiver, resulting in a lower power return than expected (Ecklund et al. 1999). Receiver saturation is evident in the 915-MHz profiler based distribution as well (note the saturation

curves in Figs. 14a,c). The western Pacific profile also exhibits a narrower distribution than the other studies. While the 99% contour compares relatively well with those from NAME and the western Amazon WR, the 10% contour corresponds to significantly higher reflectivity than those profiles, resembling that of Darwin. This means that convection in NAME and the western Amazon WR is on average weaker than convection in the other regions. The Darwin convective profile shows the highest reflectivity, indicated by the 99% contours, but the weakest vertical reflectivity gradient between 4 and 7 km (likely due to the profile's lower vertical resolution). The NAME convective profile is most similar to the western Amazon WR profile. The convective CFD for the ER (Cifelli et al. 2004, not shown) exhibits reflectivity contours approximately 4 dBZ lower than that of the WR below 5 km, so the NAME CFD compares more favorably with that of the WR.

## 5. Discussion

The primary focus of this study was to assess the vertical structure and kinematics of precipitating cloud

systems during the NAME field campaign utilizing the NOAA S-band profiler. Assessing MCS vertical structure is important in understanding how the distribution of latent heating affects the atmospheric circulation and how to better parameterize precipitating cloud systems in numerical models (Williams et al. 1995).

Case studies of three NAME rainfall events observed by the S-band profiler were described, which included the use of a simple HID algorithm based on reflectivity and temperature only. The algorithm required accurate estimates of S-band profiler reflectivity with respect to S-Pol but allowed for assessment of HID over the profiler site at the profiler's native resolution: significantly higher temporal and vertical resolution than S-Pol could provide. The simplified HID algorithm proved effective, showing similar structure within convective systems as that of the more sophisticated fuzzy logic-based S-Pol HID. However, the simplified algorithm lacked the ability to identify ice hydrometeors below the base of the melting layer (as they melt). Furthermore, convective systems appeared to reach greater heights with S-Pol measurements than with the profiler, because the profiler measured lower reflectivity than S-Pol in ice regions. This sometimes led to differences in diagnosed HID between the two platforms at upper levels, where the profiler-based HID algorithm would diagnose dry snow and that of S-Pol would diagnose dry graupel. These differences in reflectivity between the profiler and the S-Pol radar are likely the result of a combination of possible issues, including pulse volume differences, calibration issues due to ice particle asymmetry, profiler attenuation in deep convection, and S-Pol brightband sidelobe contamination (Cifelli et al. 1996; Gage et al. 2000; Williams et al. 2007; Campos et al. 2008). These hypotheses remain to be proven, however, and future work is needed to address this problem. Still, this study revealed the usefulness of a reflectivity- and temperature-based HID algorithm when combined with profiler measurements in a tropical environment. The profiler measurements were successfully put into context with those of S-Pol, and they allowed for viewing the vertical structure of North American monsoon convective systems in great detail. Distinct features were identified within convective, stratiform, and mixed stratiform-convective precipitation, consistent with those found by previous studies of tropical precipitation (e.g., Williams et al. 1995; Ecklund et al. 1999; White et al. 2002, 2003; May and Keenan 2005). Stratiform rain exhibited a reflectivity bright band and strong Doppler velocity gradient within the melting layer, and was characterized by wet snow in the melting layer, dry snow aloft, and rain and drizzle below 4 km. Convective rainfall exhibited high reflectivity and Doppler velocities that exceeded 3 and  $-10 \text{ m s}^{-1}$

in updrafts and downdrafts, respectively. Low-density graupel persisted above the melting layer, often extending to 10 km, with high-density graupel observed near the melting level. S-Pol surveillance scan-based HID revealed a similar structure. However, with lower vertical resolution it failed to identify any wet snow within the melting layer. Doppler velocity signatures suggested that updrafts and downdrafts were often tilted, though estimating the degree of tilt would have required a more three-dimensional view of the vertical velocity structure within the passing storms.

The profiler-based convective events encompassed every regime described by Lang et al. (2007) except for regime B. However, it should be noted that distinct microphysical-kinematic differences between the various regimes could not be made because of the spatial sampling restrictions of the S-band profiler (both in time and space relative to the evolution of each system).

Accumulated frequency distributions of profiler reflectivity were analyzed for the stratiform and convective regimes. The NAME distributions were similar to those from the western Pacific during TOGA COARE, northern Australia (Steiner et al. 1995), and the western Amazon (Cifelli et al. 2004).

*Acknowledgments.* The authors want to thank all of the NCAR engineers, technicians, and field scientists, as well as Robert Bowie of the CSU-CHILL radar staff who contributed to the successful S-Pol operation during NAME. Bob Rilling of NCAR EOL led initial quality control and distribution of the radar data, and various members of the CSU radar group performed further quality control on the S-Pol dataset. Dr. Timothy Lang of CSU created the final quality controlled S-Pol datasets and provided helpful comments to help improve the quality of this manuscript. Thanks go to all of those who installed and maintained hardware and collected the observations made during NAME at the NOAA field site. Last, we express our gratitude to Dr. Matthias Steiner of NCAR for supplying TOGA C-band radar reflectivity data from Darwin, Australia. This research was funded by NOAA Grant NA17RJ1228, NOAA Office of Global Programs (OGP) Grant GC04-064, and National Science Foundation (NSF) Grant ATM-0340544 from the Mesoscale Dynamics and Meteorology Program.

## APPENDIX

### Precipitation-Type Classification Algorithm

The precipitation regime classification algorithm created for this study was modeled after that used by Williams

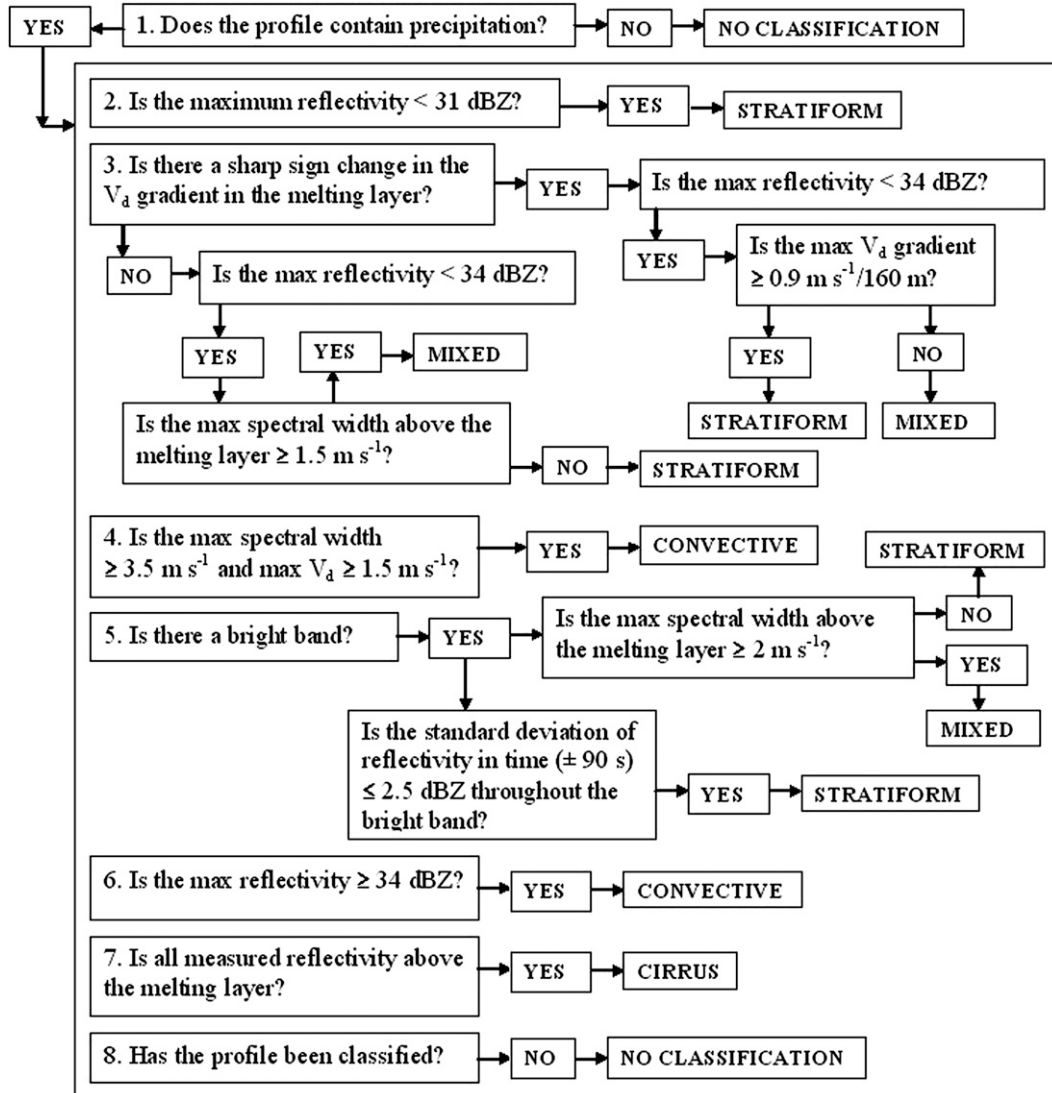


FIG. A1. The precipitation regime classification algorithm used in this study, modified from that used by Williams et al. (1995). The algorithm consists of a hierarchy (larger number classifications outweigh smaller number classifications) of possible classifications that place a profile of precipitation into one of five categories: 1) stratiform, 2) convective, 3) mixed stratiform–convective, 4) cirrus, and 5) unclassifiable.

et al. (1995) and is shown in Fig. A1. There were four classifications: 1) stratiform, 2) convective, 3) mixed stratiform–convective, and 4) nonprecipitating lofted clouds or cirrus. The algorithm consisted of a hierarchy of classification choices that began with general and progressed toward more specific requirements. Each classification option was considered to be of higher precedence than all options given before it (numbered in Fig. A1). This format allowed for nearly every data profile to be classified. After all profiles were initially classified, they were quality checked using another hierarchy technique. This quality check consisted of four loops. First, all

individual profiles originally classified as nonconvective that were surrounded by convective profiles were reclassified as convective. Second, all individual profiles originally classified as nonmixed stratiform–convective that were surrounded by mixed stratiform–convective profiles were reclassified as mixed stratiform–convective. Finally, all individual profiles originally classified as nonstratiform that were surrounded by stratiform profiles were reclassified as stratiform. The algorithm proved effective, requiring manual classification of only 35 profiles of the entire S-band profiler dataset that were misclassified by the algorithm.

## REFERENCES

- Atlas, D., and C. R. Williams, 2003: The anatomy of a continental tropical convective storm. *J. Atmos. Sci.*, **60**, 3–15.
- Battan, L. J., 1973: *Radar Observations of the Atmosphere*. University of Chicago Press, 279 pp.
- Bringi, V. N., and V. Chandrasekar, 2001: *Polarimetric Doppler Weather Radar: Principles and Applications*. Cambridge University Press, 636 pp.
- Compos, E. F., W. Hocking, and F. Fabry, 2008: Evaluating the effects of height-variable reflectivity and antenna sidelobes on the radar equation. *J. Atmos. Oceanic Technol.*, **25**, 1469–1476.
- Cifelli, R., and S. A. Rutledge, 1994: Vertical motion structure in Maritime Continent Mesoscale Convective Systems: Results from a 50-MHz profiler. *J. Atmos. Sci.*, **51**, 2631–2652.
- , —, D. J. Boccippio, and T. Matejka, 1996: Horizontal divergence and vertical velocity retrievals from Doppler radar and wind profiler observations. *J. Atmos. Oceanic Technol.*, **13**, 948–966.
- , L. Carey, W. A. Petersen, and S. A. Rutledge, 2004: An ensemble study of wet season convection in Southwest Amazonia: Kinematics and implications for diabatic heating. *J. Climate*, **17**, 4692–4707.
- Doviak, R. J., and D. S. Zrnić, 1993: *Doppler Radar and Weather Observations*. 2nd ed. Academic Press, 562 pp.
- Ecklund, W. L., C. R. Williams, P. E. Johnston, and K. S. Gage, 1999: A 3-GHz profiler for precipitating cloud studies. *J. Atmos. Oceanic Technol.*, **16**, 309–322.
- Gage, K. S., C. R. Williams, and W. L. Ecklund, 1994: UHF wind profilers: A new tool for diagnosing tropical convective cloud systems. *Bull. Amer. Meteor. Soc.*, **75**, 2289–2294.
- , —, —, and P. E. Johnston, 1999: Use of two profilers during MCTEX for unambiguous identification of Bragg scattering and Rayleigh scattering. *J. Atmos. Sci.*, **56**, 3679–3691.
- , —, P. E. Johnston, W. L. Ecklund, R. Cifelli, A. Tokay, and D. A. Carter, 2000: Doppler radar profilers as calibration tools for scanning radars. *J. Appl. Meteor.*, **39**, 2209–2222.
- Gochis, D. J., C. J. Watts, J. Garatuza-Payan, and J. Cesar-Rodriguez, 2007: Spatial and temporal patterns of precipitation intensity as observed by the NAME event rain gauge network from 2002 to 2004. *J. Climate*, **20**, 1734–1750.
- Higgins, W., and Coauthors, 2006: The NAME 2004 field campaign and modeling strategy. *Bull. Amer. Meteor. Soc.*, **87**, 79–94.
- Joss, J., and A. Waldvogel, 1970: Raindrop size distribution and Doppler velocities. Preprints, *14th Conf. on Radar Meteorology*, Tucson, AZ, Amer. Meteor. Soc., 153–156.
- Lang, T. J., R. Cifelli, L. Nelson, S. W. Nesbitt, G. Pereira, S. A. Rutledge, D. Ahijevych, and R. Carbone, 2005: Radar observations during NAME 2004. Part I: Data products and quality control. Preprints, *32nd Conf. on Radar Meteorology*, Albuquerque, NM, Amer. Meteor. Soc., JP3J.6.
- , D. A. Ahijevych, S. W. Nesbitt, R. E. Carbone, S. A. Rutledge, and R. Cifelli, 2007: Radar-observed characteristics of precipitating systems during NAME 2004. *J. Climate*, **20**, 1713–1733.
- Liu, H., and V. Chandrasekar, 2000: Classification of hydrometeors based on polarimetric radar measurements: Development of fuzzy logic and neurofuzzy systems, and in situ verification. *J. Atmos. Oceanic Technol.*, **17**, 140–164.
- Locatelli, J. D., and P. V. Hobbs, 1974: Fall speeds and masses of solid precipitation particles. *J. Geophys. Res.*, **79**, 2185–2197.
- May, P. T., and T. D. Keenan, 2005: Evaluation of microphysical retrievals from polarimetric radar with wind profiler data. *J. Appl. Meteor.*, **44**, 827–838.
- Nesbitt, S. W., D. J. Gochis, and T. J. Lang, 2008: The diurnal cycle of clouds and precipitation along the Sierra Madre Occidental observed during NAME-2004: Implications for warm season precipitation estimation in complex terrain. *J. Hydrometeorol.*, **9**, 728–743.
- Rowe, A. K., S. A. Rutledge, T. J. Lang, and S. A. Saleeby, 2008: Elevation-dependent trends in precipitation observed during NAME. *Mon. Wea. Rev.*, **136**, 4962–4979.
- Steiner, M., R. A. Houze Jr., and S. E. Yuter, 1995: Climatological characterization of three-dimensional storm structure from operational radar and rain gauge data. *J. Appl. Meteor.*, **34**, 1978–2007.
- White, A. B., D. J. Gottas, E. T. Strem, F. M. Ralph, and P. J. Neiman, 2002: An automated brightband height detection algorithm for use with Doppler radar spectral moments. *J. Atmos. Oceanic Technol.*, **19**, 687–697.
- , P. J. Neiman, F. M. Ralph, D. E. Kingsmill, and P. O. Persson, 2003: Coastal orographic rainfall processes observed by radar during the California Land-Falling Jets Experiment. *J. Hydrometeorol.*, **4**, 264–282.
- Williams, C. R., W. L. Ecklund, and K. S. Gage, 1995: Classification of precipitating clouds in the Tropics using 915-MHz wind profilers. *J. Atmos. Oceanic Technol.*, **12**, 996–1012.
- , A. B. White, K. S. Gage, and F. M. Ralph, 2007: Vertical structure of precipitation and related microphysics observed by NOAA profilers and TRMM during NAME 2004. *J. Climate*, **20**, 1693–1712.